Ag2O nanoparticle/TiO2 nanobelt heterostructures with remarkable photo-response and photocatalytic properties under UV, visible and near-infrared irradiation

Na Wei, Hongzhi Cui*, Qiang Song, Liqiang Zhang, Xiaojie Song, Ke Wang, Yanfeng Zhang, Jian Li, Jing Wen, Jian Tian*

School of Materials Science and Engineering, Shandong University of Science and Technology, Qingdao 266590, China

ARTICLE INFO

ABSTRACT

Finding a novel photocatalyst that can operate over a broad range of wavelengths from UV to near-infrared (NIR) holds great potential for diverse uses. Here, an Ag2O nanoparticle/TiO2 nanobelt heterostructure with enhanced photocatalytic performance of degrading methyl orange (MO) under UV, visible and NIR irradiation is prepared. Such an excellent photocatalytic performance is ascribed to the synergistic effects, including highly dispersed Ag2O nanoparticles on the surface of TiO2 nanobelts and efficient charge separation efficiency induced by the heterostructure between Ag2O and TiO2. Finally, a possible photocatalytic mechanism is proposed for this novel photocatalyst. This current work can afford a new paradigm for the full utilization of solar light.

© 2016 Elsevier B.V. All rights reserved.

1. Introduction

Inspired by the wide and effective utilization of solar energy in nature, photocatalytic water purification has proven to be an efficient, green and promising remedial technology for detoxifying a wide variety of organic pollutants into innocuous products (e.g. CO_2, H_2O) [1–4]. Of the well-known semiconductor photocatalysts, TiO_2 has proven itself as a representative and extensively used material, owing to its photocatalytic ability, nontoxicity, and low-cost [5–7]. However, TiO_2 possesses a large band gap of 3.2 eV and is only active under UV light, which accounts for only 5% of the total solar spectrum [8,9]. Naturally, research efforts have focused on modifying TiO_2 to enable absorption of lower-energy spectra, particularly on extension of the photocatalyst spectral response range to the visible-light region [10–14]. However, about 50% of near-infrared (NIR) light remains beyond efficient use, the harnessing of NIR photons is therefore an important challenge for development of photocatalysis.

Up to now, the investigation about NIR light photocatalysts has focused mainly on using narrow band gap semiconductors (e.g., In_2S_3 [15], WS_2 [16], $Cu_2(OH)PO_4$ [17]), NIR responsive

dye sensitization (e.g., $CuPc/Bi_2MoO_6$ [18] and $Zn-tri-PcNc/gC_3N_4$ [19]), and the introduction of rare earth doped upconversion materials(e.g., $CQDs/Cu_2O$ [20], $NaYF_4:Yb^{3+},Tm^{3+}@TiO_2$ [21] and $Er^{3+}/Yb^{3+}-(CaF_2@TiO_2)$ [22]). However, the upconversion materials usually absorb NIR light and emit UV or visible light at a certain wavelength. For example, the upconversion photocatalyst of $BiVO_4/CaF_2:Er^{3+},Tm^{3+},Yb^{3+}$ presents the photocatalytic performance under NIR irradiation, mainly by harvesting the upconversion emissions of UV (361 and 379 nm), violet (408 nm), and blue (485 nm) [23]. In addition, the above single narrow band gap semiconductors only absorb NIR light, while their NIR photocatalytic efficiencies are not very high due to the rapid recombination of the photogenerated electron–hole pairs. Therefore, it is highly interesting and a great challenge to explore photocatalytic materials that are not only activated by a broad solar light spectrum from UV to NIR light, but which also possess higher charge separation efficiency.

Herein, we first synthesized UV, visible and NIR lights driven Ag_2O nanoparticles photocatalysts. TiO_2 nanobelts were used as a supporting material, leading to homogeneous dispersion of the prepared Ag_2O nanoparticles on its surface to form spectrum-versatile UV, visible and NIR activities of Ag_2O nanoparticle/TiO_2 nanobelt heterostructures. The photocatalytic performance of the catalysts was evaluated by decomposing methyl orange aqueous solution under UV, visible and NIR irradiation. Subsequently, a

possible broad solar spectrum photocatalytic mechanism of Ag_2O nanoparticle/TiO_2 nanobelt heterostructures was proposed.

2. Experimental procedure

2.1. Chemicals

Titania P25 (TiO_2), sodium hydroxide (NaOH), hydrochloric acid (HCl), and silver nitrate ($AgNO_3$) were used of analytical grade and without further purification. Deionized water was used for preparation of all aqueous solutions.

2.2. Preparation of TiO_2 nanobelts

TiO_2 nanobelts were synthesized by a hydrothermal procedure. First, P25 (1 g) and 200 mL of 10 M NaOH aqueous solutions were homogeneously mixed together. The obtained mixture was transferred to four 50 mL Teflon-lined autoclaves and heated at 200 °C for 72 h. Then, the fabricated products were collected, rinsed thoroughly with distilled water and dissolved into a 0.1 M HCl solution for 48 h. The obtained $H_2Ti_3O_7$ nanobelts were washed with deionized water several times, and dried in the oven at 70 °C overnight. Finally, TiO_2 nanobelts were obtained by annealing the $H_2Ti_3O_7$ nanobelts at 600 °C for 2 h.

2.3. Preparation of Ag_2O nanoparticle/TiO_2 nanobelt heterostructures

Ag_2O nanoparticle/TiO_2 nanobelt heterostructures were prepared by a simple chemical precipitation method and the weight ratio was fixed to 4:1. In a typical process, 0.1 g TiO_2 nanobelts were dispersed in 50 mL of distilled water, and 0.59 g of $AgNO_3$ was added to the suspension. After, the mixture was stirred magnetically for 30 min, 50 mL of 0.2 M NaOH was dropped to the above mixture of $AgNO_3$ and TiO_2. The amount of NaOH was more than sufficient to precipitate Ag_2O from the added $AgNO_3$, and the final pH 14. Finally, The as-prepared Ag_2O nanoparticle/TiO_2 nanobelt heterostructures were washed with deionized water and dried in the oven at 50 °C overnight. For comparison, pure Ag_2O was also obtained in the absence of TiO_2 nanobelts during the process of preparation of Ag_2O nanoparticle/TiO_2 nanobelt heterostructures.

2.4. Sample characterization

X-ray diffraction (XRD) patterns were recorded on a Japan D/Max 2500PC Rigaku X-ray diffractometer with Cu Kα radiation ($\lambda = 0.15405$ nm) in the range of 20–70° (2θ). The morphologies of the samples were obtained using scanning electron microscopy (SEM, NANO FEI-450). The high-resolution transmission electron microscopy (HRTEM) images were obtained using a JEOL 2100 microscope. X-ray photoelectron spectrometry (XPS) measurements were performed on a Thermo ESCALAB 250XI XPS system with a source and a charge neutralizer. Fourier transform infrared (FTIR) spectra were recorded on a Magna-IR 750 FTIR spectrometer (Thermo Scientific) with a spectral resolution of 2 cm^{-1}. For in situ Raman measurements, the as-prepared samples powders were handed pressed on a glass substrate by a flat spoon. The photoluminescence (PL) spectra were measured with a Raman spectroscope (HR 800, JY) under a laser excitation of 325 nm. Surface areas were determined from nitrogen adsorption–desorption isotherms at liquid nitrogen temperature using a Quantachrome surface area analyzer. The Brunauer–Emmett–Teller (BET) method was used for the surface area calculation. The electronspin resonance (ESR) signals of hydroxyl radicals spin-trapped by aspin-trap reagent 5,5-dimethyl- 1-pyrroline-N-oxide (DMPO) were examined on a Bruker model ER200-SRC spectrometer equipped with a
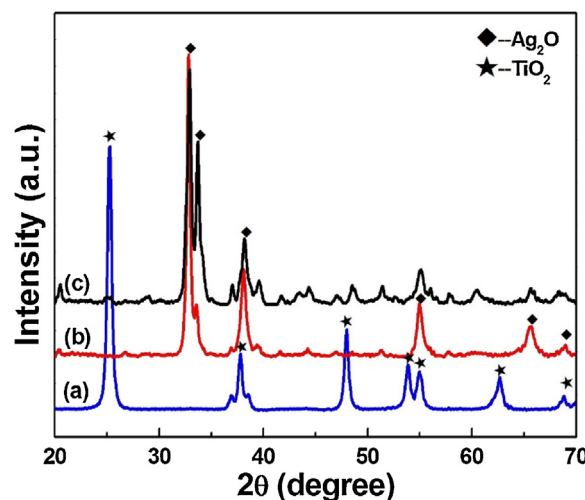

Fig. 1. XRD patterns of the as-synthesized products: (a) TiO_2 nanobelts, (b) Ag_2O nanoparticles, and (c) Ag_2O nanoparticle/TiO_2 nanobelt heterostructures.

quanta-Ray Nd:YAG laser system as the irradiation source. Visible light of 420 nm was used to irradiate the sample.

Photocurrent measurements were carried out using the conventional three electrode setup connected to an electrochemical station (Zennium). In this electrochemical system, the prepared catalyst/ITO was used as the working electrode; a Pt wire was used as the counter electrode and an Ag/AgCl electrode (saturated KCl) was used as the reference electrode. The electrolyte was 0.5 M Na_2SO_4 aqueous solution. A 633 nm LED (90 W/cm^{-2}) lamp served as a light source. The measurements were carried out at a constant potential of 0.2 V to the working electrode.

2.5. Photocatalytic activity test

The photocatalytic performance was evaluated by the degradation of MO solution under various light irradiation and experiments were carried out using a model XPA photocatalytic reactor (Xujiang Electromechanical Plant, Nanjing, China). A 300 W mercury lamp with a maximum emission at 356 nm, a 350 W xenon lamp with a UV cutoff filter ($\lambda > 420$ nm), and a 5 W 840 nm LED were used as UV, visible, and NIR light sources, respectively. The 350 W xenon lamp without cutoff filter was used as a simulated solar light source. In a typical photocatalytic experiment, 10 mg of sample was dispersed into 10 mL MO (20 mg/L) solution with constant stirring. The suspension was stirred in the dark for 30 min to reach the adsorption–desorption equilibrium before irradiation. At varied irradiation time intervals, an aliquot of the mixed solution was collected and centrifuged, and the residual MO concentration in the supernatant was analyzed by UV–vis-NIR spectroscopic measurements (Hitachi UV-3101).

3. Results and discussions

3.1. Characterization results

The crystal structures of the as-prepared TiO_2 nanobelts, Ag_2O nanoparticles and Ag_2O nanoparticle/TiO_2 nanobelt heterostructures have been characterized by XRD, as illustrated in Fig. 1. In curve a, the diffraction peaks at 25.28°, 36.95°, 37.80°, 38.58°, 48.05°, 53.89°, 55.06°, 62.69° and 68.76° correlate to anatase TiO_2 (JCPDS 21–1272) [24]. In pure Ag_2O nanoparticles (curve b), the diffraction peaks at 2θ of 26.7°, 32.8°, 38.1°, 54.9°, 65.4° and 68.8° are attributed to the respective (110), (111), (200), (220), (311), and (222) planes of the cubic Ag_2O crystal phase (JCPDS 41–1104) [25].
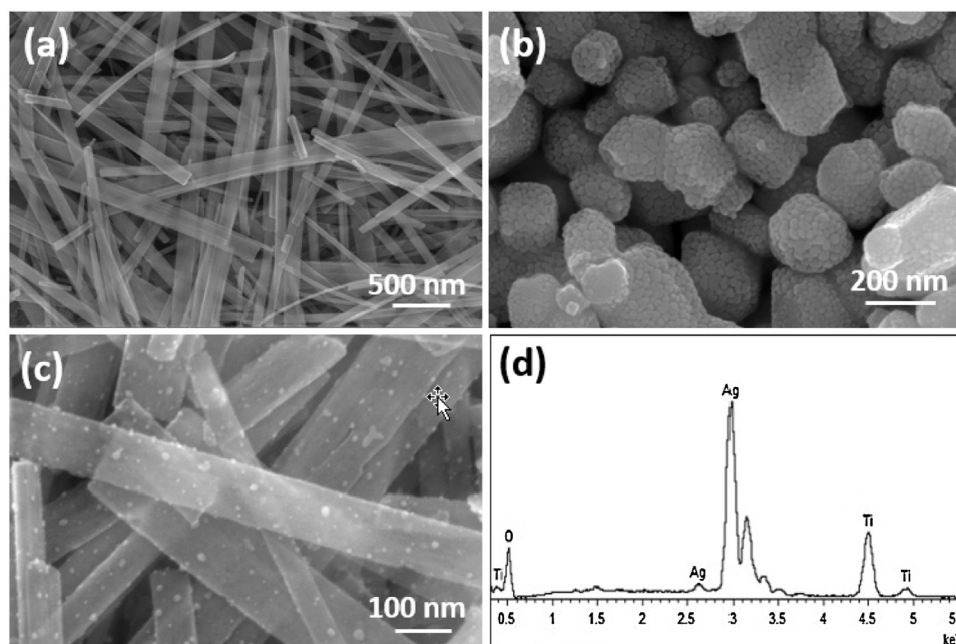
Fig. 2. SEM images of the as-synthesized products: (a) TiO_2 nanobelts, (b) Ag_2O nanoparticles, and (c) Ag_2O nanoparticle/TiO_2 nanobelt heterostructures; (d) EDS spectrum of Ag_2O nanoparticle/TiO_2 nanobelt heterostructures.
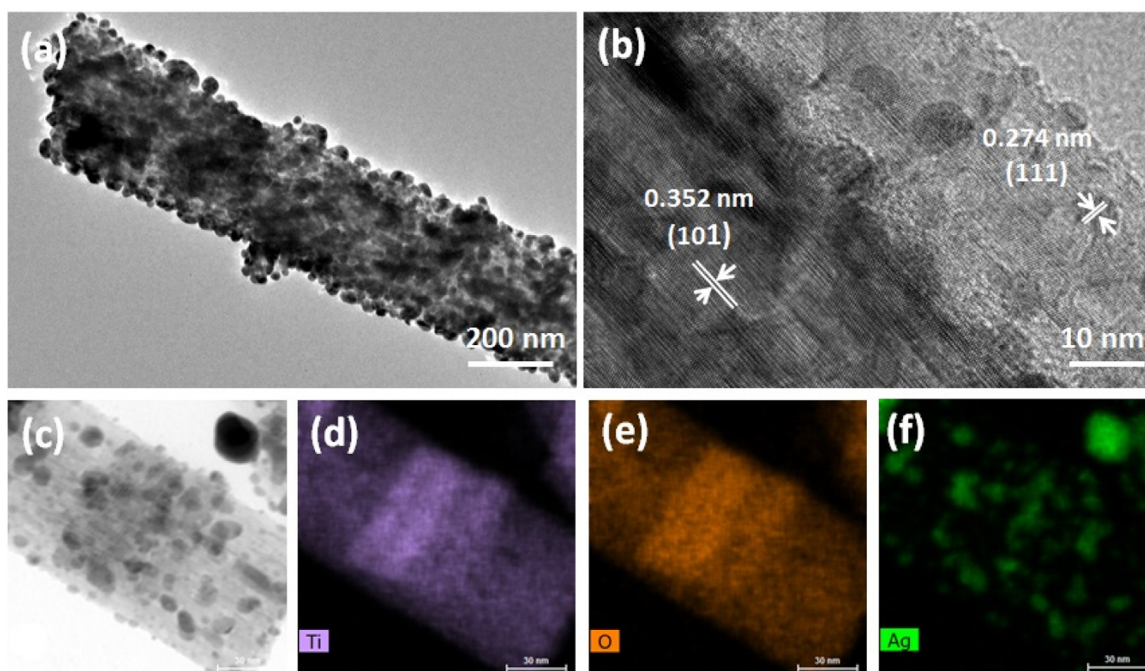

Fig. 3. Typical TEM (a), HRTEM (b) and (c–f) EDS mapping images of the as-prepared Ag_2O nanoparticle/TiO_2 nanobelt heterostructures.

For the Ag_2O/TiO_2 heterostructure (curve c), all the peaks can be assigned to TiO_2 or Ag_2O, and no other impurity peak was observed.

Both distribution and morphology of Ag_2O nanoparticles around TiO_2 nanobelts have been confirmed by scanning electron microscopy (SEM), as shown in Fig. 2. The results of SEM images in Fig. 2a show that the TiO_2 nanobelts are 50–200 nm in width and up to several micrometers in length [26]. The size range of Ag_2O nanoparticles is 100–500 nm and a plentiful aggregation of Ag_2O micrograins with a dimension of less than 10 nm appears in Fig. 2b. As shown in Fig. 2c, Ag_2O nanoparticles are uniformly loaded on TiO_2 nanobelts, while their size is much smaller than that of the

Ag_2O nanoparticles in Fig. 2b. It is likely that TiO_2 nanobelts provide numerous nucleation sites for the growth of Ag_2O nanoparticles, leading to homogeneous dispersion of Ag_2O nanoparticles on the TiO_2 nanobelts with a smaller size [26]. As determined by the BET method at liquid-nitrogen temperature, the surface areas of TiO_2 nanobelts is $34.69\,m^2g^{-1}$, while the average surface area of the Ag_2O/TiO_2 heterostructures decreases dramatically to $7.70\,m^2g^{-1}$. This is due to the fact that partial obstruction of the TiO_2 void space by the growth of Ag_2O on the surface of TiO_2. Compared with pure Ag_2O (about $4.22\,m^2g^{-1}$), the surface areas of heterostructures increase, implying that TiO_2 can also facilitate dispersion
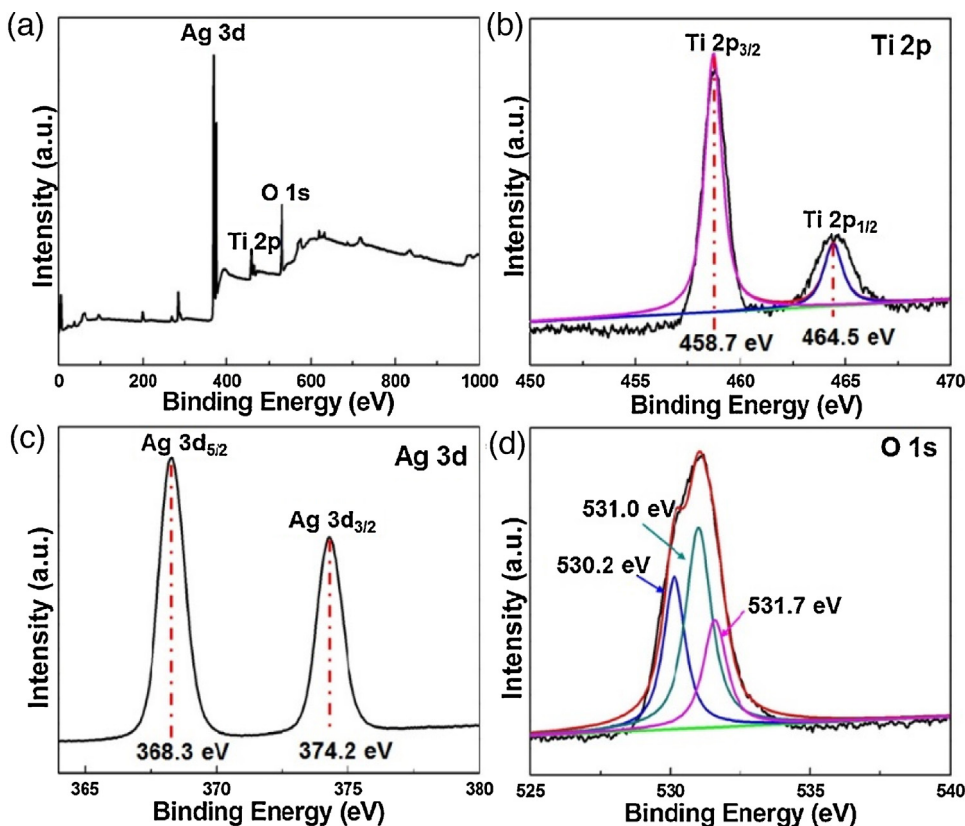
Fig. 4. XPS spectra in Ag$_2$O nanoparticle/TiO$_2$ nanobelt heterostructures: (a) full spectrum, (b) Ti 2p, (c) Ag 3d, and (d) O 1s.

of Ag$_2$O nanoparticles on the TiO$_2$ nonobelt surfaces (Table S1). Fig. 2d presents the energy-dispersive X-ray spectroscopy (EDS) of Ag$_2$O/TiO$_2$ heterostructures, which indicates the presence of elements Ti, Ag and O in the Ag$_2$O/TiO$_2$ heterostructures.

Typical transmission electron microscopy (TEM) images were used to further confirm the formation of the Ag$_2$O/TiO$_2$ heterostructures, as shown in Fig. 3a. As well, the high-resolution TEM image reveals the simultaneous presence of both crystalline TiO$_2$ and Ag$_2$O (Fig. 3a). The interplanar spacing of 0.274 nm corresponds to the (111) plane of Ag$_2$O, while 0.352 nm is attributed to the (101) plane of anatase TiO$_2$ (Fig. 3b). The distinguished interfaces between lattice fringes of Ag$_2$O and TiO$_2$ indicate formation of a heterostructure, which is expected to significantly increase charge separation efficiency and to enhance the photocatalytic activity [27]. Energy dispersive X-ray spectrometry (EDS) mapping analysis of the Ag$_2$O/TiO$_2$ heterostructures also confirms that Ag$_2$O nanoparticles are successfully assembled onto the surface of TiO$_2$ nanobelts (Fig. 3c–f).

Both chemical composition and elemental chemical status of Ag$_2$O/TiO$_2$ heterostructures were analyzed by XPS. Fig. 4a displays the XPS survey spectra of Ag$_2$O/TiO$_2$ heterostructures, which is composed only of Ag, Ti, and O elements. The XPS spectra of Ti 2p indicate two peaks at ∼464.5 eV and ∼458.7 eV, as shown in Fig. 4b, which correspond respectively to the typical binding energies for Ti 2p$_{1/2}$ and Ti 2p$_{3/2}$ in TiO$_2$ [28]. The Ag 3d peaks of Ag$_2$O are located at ∼368.3 and ∼374.2 eV (Fig. 4c), which correspond respectively to the Ag 3d$_{5/2}$ and Ag 3d$_{3/2}$ binding energies [29]. It indicates that only Ti^{4+} and Ag$^+$ exist as TiO$_2$ and Ag$_2$O in the prepared composite, which supports the results of XRD and EDS. In this case, oxygen on the sample surface exists in the form of the binding energies at 531.7 eV, 531.0 eV and 530.2 eV (Fig. 4d). The main peaks at 530.2 eV and 531.0 eV could be ascribed to the oxygen lattices in TiO$_2$ and Ag$_2$O, respectively. Beneficial to improvement of pho-
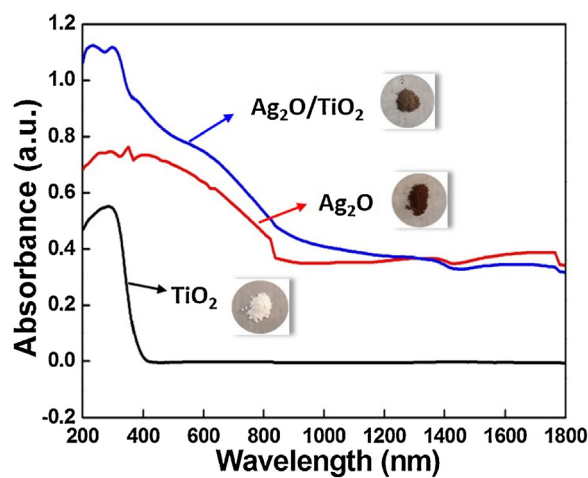

Fig. 5. UV–vis–NIR diffuse reflectance spectra (DRS) of TiO$_2$ nanobelts, Ag$_2$O nanoparticle/TiO$_2$ nanobelt heterostructures, and Ag$_2$O nanoparticles. Inset shows the colors of the corresponding samples.

tocatalytic activity [30–32], the external −OH group or the water molecule adsorbed on the surface of the Ag$_2$O/TiO$_2$ heterostructure sample is reflected by a peak at 531.7 eV.

3.2. Photocatalytic performance

The optical properties of the as-prepared pure TiO$_2$ nanobelts, Ag$_2$O nanoparticles, and Ag$_2$O/TiO$_2$ heterostructures were investigated by UV–vis–NIR DRS (Fig. 5). As shown in Fig. 5, TiO$_2$ nanobelts exhibit a steep absorption edge at ∼390 nm (black line), that is to say, the bandgap energy of 3.16 eV and is consistent with the reported data [33]. DRS of pure Ag$_2$O nanoparticles (red line), it
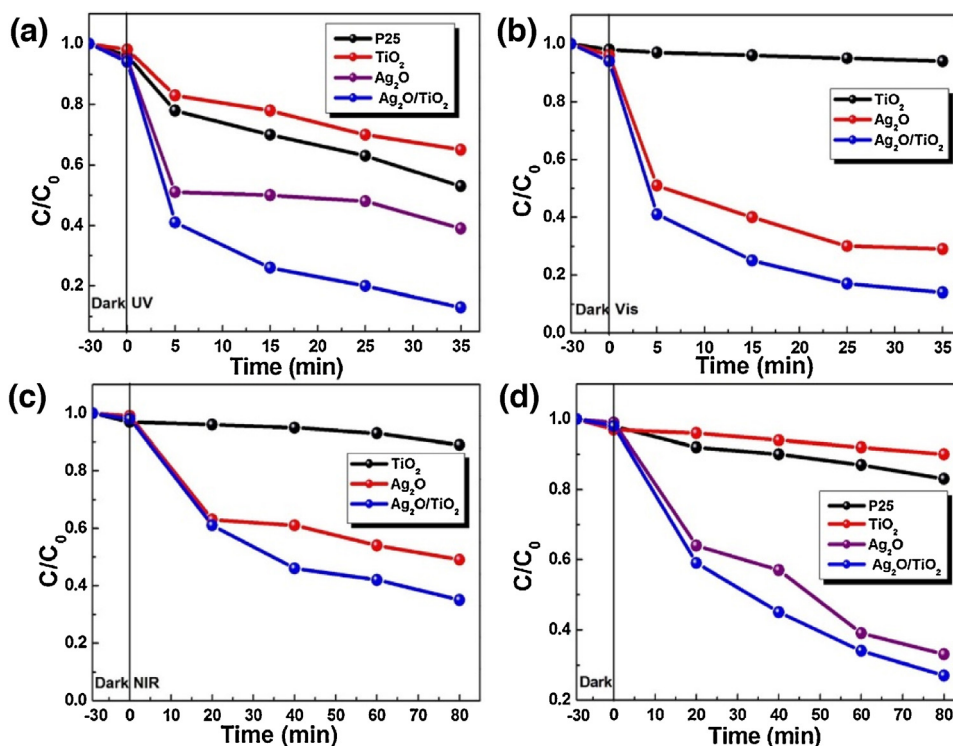
Fig. 6. Photocatalytic degradation of MO aqueous solution by TiO_2 nanobelts, Ag_2O nanoparticles and Ag_2O nanoparticle/TiO_2 nanobelt heterostructures under (a) UV light, (b) visible light, (c) NIR light and (d) simulated sunlight irradiation.
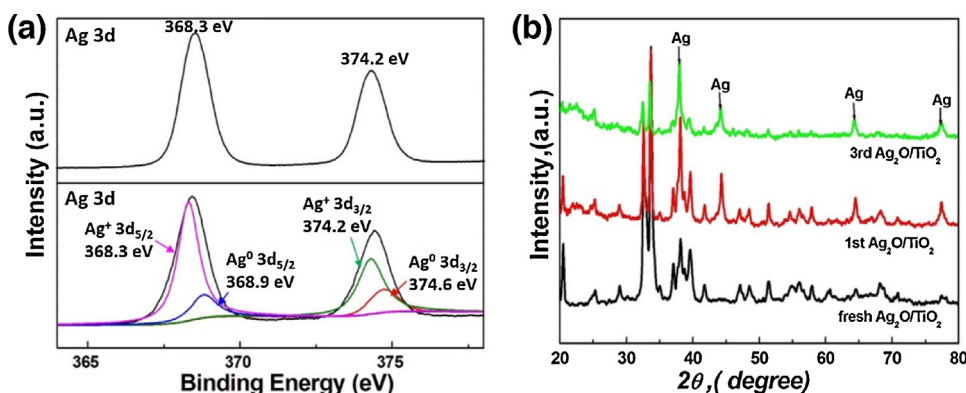

Fig. 7. Ag 3d XPS spectra (a) and XRD patterns (b) of Ag_2O/TiO_2 heterostructure before and after the repeated photocatalytic degradation experiments under NIR light irradiation.

exhibits a broad and strong light absorption, while the absorption edge extends to ~956 nm (corresponding bandgap energy of 1.19 eV), which is in agreement with the reported value of 960 nm [34]. After Ag_2O nanoparticles are assembled on the surface of TiO_2 nanobelts, the visible and NIR light responses of the composites are significantly improved in comparison with TiO_2 nanobelts. Because Ag_2O and Ag_2O/TiO_2 composites exhibit a broad and strong light absorption in the whole UV–vis–NIR range of 200–1800 nm, their probable photocatalytic activity of them in the UV–vis–NIR region is suggested. In addition, heavy Ag_2O/TiO_2 heterostructure absorption in the red shift enhances photoexcitation efficiency and its photocatalytic activity.

Photodegradation of methyl orange (MO) under UV, visible, NIR light and simulated solar light irradiation (Fig. 6) was applied to evaluate photocatalytic activities of the prepared Ag_2O/TiO_2 heterostructures. For comparison, Ag_2O nanoparticles, TiO_2 nanobelts, and P25 were used as photocatalytic references under the same experimental conditions. As shown in Fig. 6a, when TiO_2, P25 and Ag_2O are added, MO concentration gradually decreases and the degradation efficiencies are 35%, 47% and 61% after 35 min of UV light irradiation, respectively. But, with the Ag_2O loaded on TiO_2, the photocatalytic activities of Ag_2O/TiO_2 heterostructures are remarkably improved, with a degradation efficiency of 87%. Again, after 35 min of visible irradiation (Fig. 6b), degradation is negligible for the TiO_2 nanobelt catalyst, due to a large band gap. Surprisingly, pure Ag_2O shows good visible light photocatalytic activity, with the degradation rate reaching 71% after 35 min. Compared to Ag_2O nanoparticles, Ag_2O/TiO_2 heterostructures show much higher degradation rates, with 86% of MO degraded after 35 min of visible light irradiation.

Even more interesting is that the Ag_2O and Ag_2O/TiO_2 heterostructures were detected as possessing a rather high NIR light photocatalytic activity. As indicated in Fig. 6c, the photodegradation of MO by Ag_2O/TiO_2 heterostructures and Ag_2O nanoparticles
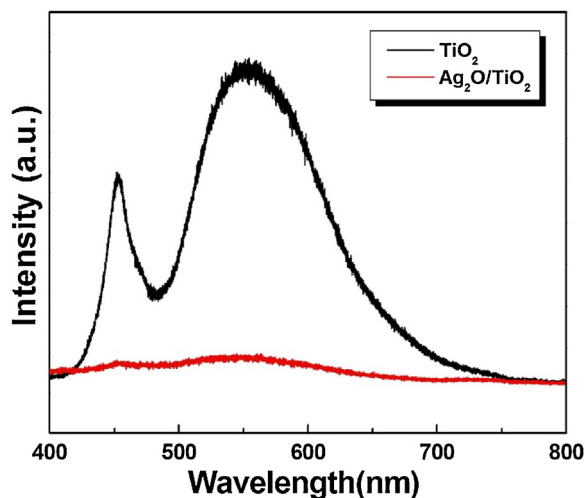
Fig. 8. Photoluminescence (PL) spectra of TiO_2 nanobelts and Ag_2O nanoparticle/TiO_2 nanobelt heterostructures, $\lambda ex = 325$ nm.
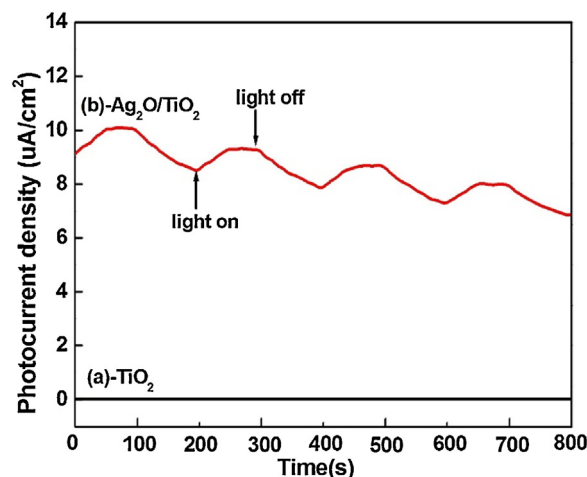

Fig. 9. Photocurrent responses of bare TiO_2 and Ag_2O nanoparticle/TiO_2 nanobelt heterostructures in the dark and under NIR light irradiation in 0.5 M Na_2SO_4 solutions.

is similar over the initial 20 min. However, Ag_2O/TiO_2 heterostructures exhibit better photocatalytic activity after extended NIR light irradiation, about 65% of MO degraded within 80 min.

Moreover, Ag_2O/TiO_2 heterostructures demonstrate exemplary photocatalytic activity under simulated sunlight irradiation. As shown in Fig. 6d, the MO degradation rate for Ag_2O/TiO_2 heterostructures increases to 73% after 80 min of simulated sunlight. In contrast, the corresponding MO degradation rates for P25, TiO_2 nanobelts and Ag_2O nanoparticles are only 17%, 10%, and 67% after 80 min of simulated sunlight irradiation.

In order to investigate the stability of Ag_2O/TiO_2 heterostructures under UV, visible and NIR light irradiation, the same samples were recycled four times after separation by centrifugation, and the results are shown in Fig. S1. Amazingly, after the excitation of UV, visible and NIR lights, the degradation rate of MO is slightly decreased after four repeated trials, which is still higher than that of TiO_2.

To further find the above reason, Ag_2O/TiO_2 heterostructures after photocatalytic reaction under NIR irradiation were characterized by XPS and XRD (Fig. 7). With the results shown in Fig. 7a, a Ag 3d peak shows a larger full width at half maximum compared with the fresh Ag_2O/TiO_2 heterostructures. The Ag $3d_{5/2}$ and $3d_{3/2}$ peaks could be further divided into two different peaks. The peaks at 368.3 eV and 374.2 eV are assigned to Ag^+ of Ag_2O, and the peaks at 368.9 eV and 374.6 eV are assigned to metallic Ag^0. Meanwhile, the Ag amount is continually increased with repeated times and simultaneously, the Ag_2O peaks are continually weakened (Fig. 7b). These results suggest that partial Ag_2O are reduced to metallic Ag in the process of photocatalytic reaction, which are responsible for the reduced activity after several recycles.

Since photoluminescent (PL) spectra emission arises from the recombination of free carriers, PL spectra are first choice to explore the mitigation, transfer and recombination processes of photogenerated electron-hole pairs in semiconductors. The PL results are presented in Fig. 8, wherein TiO_2 clearly exhibits much stronger intensity than Ag_2O/TiO_2 heterostructures, further indicating that the recombination of photo-induced electrons and holes in Ag_2O/TiO_2 heterostructures can be effectively inhibited, while photocatalytic activity can be further improved.

In addition to PL, photocurrent response can also provide evidence for the separation rate of the photogenerated e^-/h^+ pairs in heterojunctions. Fig. 9 illustrates the photocurrent responses of bare TiO_2 and Ag_2O/TiO_2 heterostructures under NIR light irradiation at 0.2 V bias versus that of SCE. Under illumination, the

photocurrent response of Ag_2O/TiO_2 heterostructures is as high as 10.1 uA/cm^2. By contrast, no significant current is observed for the bare TiO_2 sample, which confirms that the narrow band gap Ag_2O can effectively absorb NIR light to offer plentiful photogenerated electrons, and thus facilitate NIR photocatalytic activity [35].

To investigate the reactive oxygen species generated during the photodegradation of the MO, and thus discover the reaction mechanism, the ESR (electron spin resonance) spin-trap technique (with DMPO, 5,5-dimethyl-1-pyrroline N-oxide) was employed on Ag_2O/TiO_2 heterostructures (Fig. 10). There is no signal when the system in the dark, while both signals of DMPO-$\bullet O_2^-$ and DMPO-$\bullet OH$ could be clearly observed once Ag_2O/TiO_2 heterostructures are irradiated under light irradiation. As well, the $\bullet O_2^-$ and $\bullet OH$ signal intensities of the system increase with extended irradiation time, as shown in Fig. 10a and b. Therefore, a dual mechanism in the photocatalytic process is predicted, involving oxidation of both $\bullet OH$ radicals and $\bullet O_2^-$ radicals.

3.3. Photocatalytic mechanism

According to the above mentioned experimental results, a possible mechanism for photocatalytic degradation of MO by the Ag_2O/TiO_2 heterostructure photocatalyst under UV, visible and NIR light is proposed, as shown in Fig. 11. The Ag_2O/TiO_2 heterostructures are believed to exhibit cooperative or synergetic effects between TiO_2 and Ag_2O. To clarify the separation and migration of e^-/h^+ pairs at the Ag_2O/TiO_2 interface, it is necessary to ascertain the respective band structures of Ag_2O and TiO_2, respectively. The conduction band (CB) edge of a semiconductor can be calculated by the following equation [36]:

$$E_{CB} = X - E_C - 0.5E_g \qquad (1)$$

wherein, X is the absolute electronegativity of a semiconductor, expressed as the geometric mean of the absolute electronegativity of constituent atoms; E_c is the energy of free electrons on the hydrogen scale (ca. 4.5 eV), and E_g is the semiconductor band gap. Fig. 11 depicts the calculated band edge positions of TiO_2 and Ag_2O, based on the estimated E_g in DRS spectra (Fig. 5). The conduction band bottom of TiO_2 is higher than that of Ag_2O, while the valence band top is lower than that of Ag_2O. In addition, an electric field can be built at the Ag_2O/TiO_2 heterojunction and along the inner electric field direction: $TiO_2 \rightarrow Ag_2O$. Considering the inner electric field and energy band structure, it is reasonable to conclude that electron transfer between TiO_2 and Ag_2O is partially restricted.
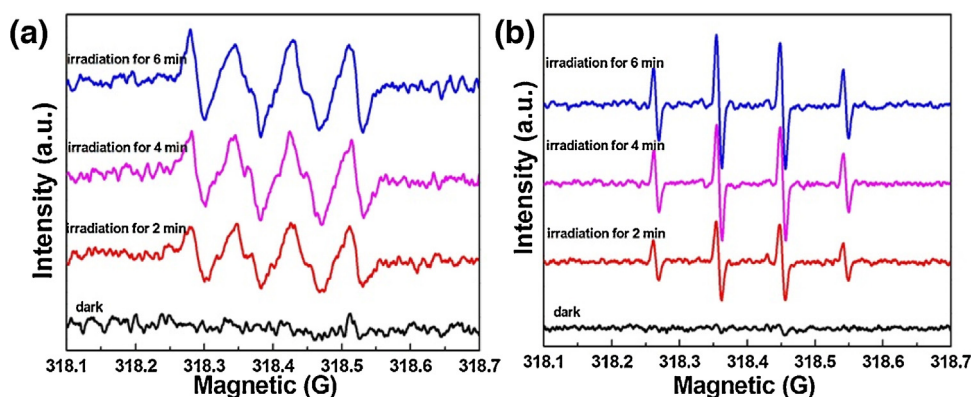
Fig. 10. DMPO spin-trapping ESR spectra of Ag$_2$O nanoparticle/TiO$_2$ nanobelt heterostructures (a) in methanol dispersion for DMPO-•O$_2^-$ and (b) in aqueous dispersion for DMPO-•OH under light irradiation.
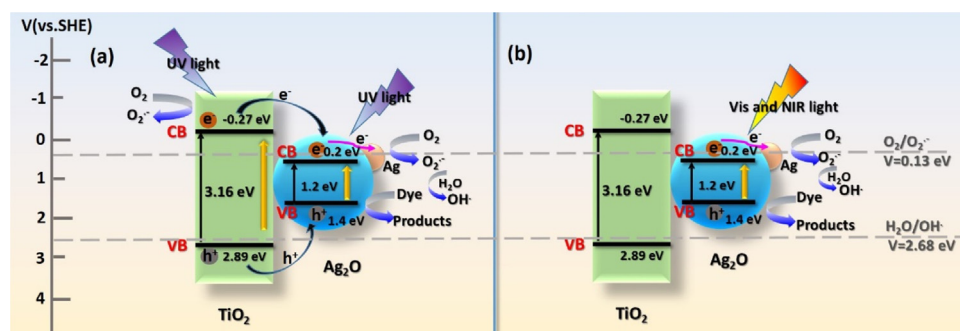

Fig. 11. Schematic diagrams for the possible photocatalytic mechanism of the Ag$_2$O nanoparticle/TiO$_2$ nanobelt heterostructures under UV–vis-NIR light irradiation.

However, hole transfer can be accelerated, causing an efficient separation of photogenerated electrons and holes while enhancing the photocatalytic activities [30,32].

On the other hand, Ag$_2$O nanoparticles are unstable and easily be reduced to metallic Ag by photogenerated electrons, as confirmed by XRD and XPS results after reaction (Fig. 7). Similar results of this self-stable Ag$_2$O mechanism have been revealed in previous works [37–39]. Due to Schottky barriers at the metal-semiconductor interface, photogenerated electrons tend to transfer from TiO$_2$ to Ag$_2$O, which efficiently inhibits the recombination of the photoexcited electrons and holes.

As shown in Fig. 11a, both TiO$_2$ and Ag$_2$O can be excited to generate electrons (e$^-$) and holes (h$^+$) under UV light irradiation, which photogenerated electrons and holes in TiO$_2$ migrate towards to Ag$_2$O, according to the above analysis of band structure. The electrons of TiO$_2$ can be further captured by Ag. Also illustrated in Fig. 11a, the captured electrons in Ag are trapped by O$_2$ to produce •O$_2^-$, then combine with H$_2$O to be further transformed into •OH. Simultaneously, photo-induced holes in the valence band of AgO transfer to the photocatalyst surface and directly oxidize the organic pollutants, resulting in markedly improved photocatalytic activity. Improved activity is due to greater positive potentials of •OH/OH$^-$ (1.99 V vs SHE), H$_2$O$_2$ (1.77 V vs SHE), O$_3$ (2.07 V vs SHE) and •OH/H$_2$O (+2.68 eV vs SHE) as compared to the VB of Ag$_2$O [30].

When the Ag$_2$O/TiO$_2$ heterostructure is irradiated by visible and NIR light, only the electrons in the VB of Ag$_2$O can be excited, as shown in Fig. 11b. The electrons in the CB of Ag$_2$O migrate to Ag to combine with oxygen, leading to the separation of carriers. In addition, the photocatalytic mechanism of photogenerated holes in Ag$_2$O under visible and NIR light are similar to irradiation by UV light (Fig. 11a).

Based on the above discussion, it can be concluded that the enhanced photocatalytic activity of the prepared Ag$_2$O/TiO$_2$ derives from three aspects. The first enhancement is the improved dispersion and smaller particle size of Ag$_2$O. Second is the improved optical absorption property arising from the heterostructure between TiO$_2$ and Ag$_2$O. Third, Ag$^+$ in Ag$_2$O is partially reduced to metallic Ag^0 by photogenerated electrons, which works as an electron pool and transfers photogenerated electrons from Ag$_2$O to combine with O$_2$, resulting in the high separation rate of photogenerated electrons and holes.

4. Conclusions

In summary, one dimensional TiO$_2$ nanobelts were successfully fabricated by a hydrothermal procedure that provides numerous nucleation sites for Ag$_2$O nanoparticles loading, thereby forming Ag$_2$O nanoparticle/TiO$_2$ nanobelt heterostructures. The novel Ag$_2$O nanoparticle/TiO$_2$ nanobelt heterostructures show highly efficient photocatalytic performance in degradation of MO degradation under UV, visible, NIR light and simulated sunlight irradiation. Such an excellent performance results from synergy, including induction of the heterostructure between TiO$_2$ and Ag$_2$O by the higher charge separation efficiency of photo-induced electron-hole pairs, plus absorption of visible and NIR light absorption due to the highly dispersed Ag$_2$O nanoparticles.

Appendix A. Supplementary data

Supplementary data associated with this article can be found, in the online version, at http://dx.doi.org/10.1016/j.apcatb.2016.05.040.

References

[1] L. Zhu, B. Wei, L.L. Xu, Z. Lü, H.L. Zhang, H. Gao, J.X. Che, CrystEngComm 14 (2012) 5705–5709.
[2] J.X. Low, J.G. Yu, Q. Li, B. Cheng, Phys. Chem. Chem. Phys. 16 (2014) 1111–1120.
[3] Y.H. Cao, Q.Y. Li, Y.Y. Xing, L.L. Zong, J.J. Yang, Appl. Surf. Sci. 341 (2015) 190–195.
[4] Y. Wang, Y.Z. Zheng, S. Lu, X. Tao, Y. J.F. Chen Che, ACS Appl. Mater. Interfaces (2015) 6093–6101.
[5] L.C. Kao, C.J. Lin, C.L. Dong, C.L. Chen, S.Y.H. Liou, Chem. Commun. 51 (2015) 6361–6364.
[6] S.I. Mogal, V.G. Gandhi, M. Mishra, S. Tripathi, T. Shripathi, P.A. Joshi, O.S. Dinesh, Ind. Eng. Chem. Res. 53 (2014) 5749–5758.
[7] P.A. Neale, K. Å. Jämting, E.O. Malley, J. Herrmann, B.I. Escher, Environ. Sci. Nano 2 (2015) 86–93.
[8] H. Ghassemi, W. Harlow, O. Mashtalir, M. Beidaghi, M.R. Lukatskaya, Y. Gogotsi, M.L. Taheri, J. Mater. Chem. A 2 (2014) 14339–14343.
[9] Q. Dong, W. Liao, B. Wang, Z.Q. Liu, RSC Adv. 5 (2015) 33869–33877.
[10] B. Xue, T. Sun, J.K. Wu, F. Mao, W. Yang, Ultrason. Sonochem. 22 (2015) 1–6.
[11] J.W.J. Hamilton, J.A. Byrne, P.S.M. Dunlop, D.D. Dionysiou, M. Pelaez, K.O. Shea, S. Damian, S.C. Pillai, J. Phys. Chem. C 118 (2014) 12206–12215.
[12] J. Tian, Y.H. Leng, H.Z. Cui, H. Liu, J. Hazard. Mater. 299 (2015) 165–173.
[13] G.Z. Zhang, F. Teng, Y.Q. Wang, P. Zhang, C.S. Gong, L.L. Chen, C.H. Zhao, E.Q. Xie, RSC Adv. 3 (2013) 24644–24649.
[14] Z.H. Zhao, J. Tian, D. Wang, X.L. Kang, Y.H. Sang, H. Liu, J.Y. Wang, S.W. Chen, R.I. Boughtond, H.D. Jiang, J. Mater. Chem. 22 (2012) 23395–23403.
[15] W.W. Gao, W.X. Liu, Y.H. Leng, X.W. Wang, X.Q. Wang, B. Hu, D.H. Yu, Y.H. Sang, H. Liu, Appl. Catal. B Environ. 176-177 (2015) 83–90.
[16] Y.H. Sang, Z.H. Zhao, M.W. Zhao, P. Hao, Y.H. Leng, H. Liu, Adv. Mater. 27 (2015) 363–369.
[17] Z.J. Li, Y. Dai, X.C. Ma, Y.T. Zhu, B.B. Huang, Phys. Chem. Chem. Phys. 16 (2014) 3267–3273.
[18] Z.J. Zhang, W.Z. Wang, D. Jiang, J.Y. Xu, Catal. Commun. 55 (2014) 15–18.
[19] X.H. Zhang, L.J. Yu, C.S. Zhuang, T.Y. Peng, R.J. Li, X.G. Li, ACS Catal. 4 (2014) 162–170.
[20] H.T. Li, R.H. Liu, Y. Liu, H. Huang, H. Yu, H. Ming, S.Y. Lian, S.T. Lee, Z.H. Kang, J. Mater. Chem. 22 (2012) 17470–17475.
[21] W. Wang, M.Y. Ding, C.H. Lu, Y.R. Ni, Z.Z. Xu, Appl. Catal. B Environ. 144 (2014) 379–385.
[22] S.Q. Huang, L. Gu, C. Miao, Z.Y. Lou, N.W. Zhu, H.P. Yuan, A.D. Shan, J. Mater. Chem. A. 1 (2013) 7874–7879.
[23] S.Q. Huang, N.W. Zhu, Z.Y. Lou, L. Gu, C. Miao, H.P. Yuan, A.D. Shan, Nanoscale 6 (2014) 1362–1368.
[24] J. Tian, Y.H. Sang, Z.H. Zhao, W.J. Zhou, D.Z. Wang, X.L. Kang, H. Liu, J.Y. Wang, S.W. Chen, H.Q. Cai, H. Huang, Small 9 (2013) 3864–3872.
[25] S.S. Ma, J.J. Xue, Y.M. Zhou, Z.W. Zhang, RSC Adv. 5 (2015) 40000–40006.
[26] W.J. Zhou, H. Liu, J.Y. Wang, D. Liu, G.J. Du, J.J. Cui, ACS Appl. Mater. Interfaces 2 (2010) 2385–2392.
[27] X.H. Hu, Q. Zhu, X.L. Wang, N. Kawazoe, Y.N. Yang, J. Mater. Chem. A 3 (2015) 17858–17865.
[28] J.H. Li, X.Y. Liu, Y.Q. Qiao, H.Q. Zhu, C.X. Ding, Colloids Surf. B Biointerfaces 113 (2014) 134–145.
[29] R.J. Zhang, J. Zhang, B.S. Wang, S.L. Zheng, H. Xia, Y. Qu, Energy Environ. Focus 4 (2015) 164–169.
[30] M. Xu, L. Han, S.J. Dong, ACS Appl. Mater. Interfaces 5 (2013) 12533–12540.
[31] W. Yua, X.J. Liu, H.P. Chu, G. Zhu, J.L. Lia, J.Y. Liu, L.Y. Niu, Z. Sun, L.K. Pan, J. Mol Catal, A Chem. 407 (2015) 25–31.
[32] L. Shi, L. Liang, J. Ma, F.X. Wang, J.M. Sun, Catal. Sci. Technol. 4 (2014) 758–765.
[33] J. Tian, P. Hao, N. Wei, H.Z. Cui, H. Liu, ACS Catal. (2015) 1–7.
[34] W. Jiang, X.Y. Wang, Z.M. Wu, X.N. Yue, S.J. Yuan, H.F. Lu, B. Liang, Ind. Eng. Chem. Res. 54 (2015) 832–841.
[35] C.B. Liua, C.H. Cao, X.B. Luo, S.L. Luo, J. Hazard. Mater. 285 (2015) 319–324.
[36] N. Liang, M. Wang, L. Jin, S.S. Huang, W.L. Chen, M. Xu, Q.Q. He, J.T. Zai, N.H. Fang, X.F. Qian, ACS Appl. Mater. Interfaces 6 (2014) 11698–11705.
[37] H.T. Ren, S.Y. Jia, Y. Wu, S.H. Wu, T.H. Zhang, X. Han, Ind. Eng. Chem. Res. 53 (2014) 17645–17653.
[38] X.F. Wang, S.F. Li, H.G. Yu, J.G. Yu, S.W. Liu, Chemistry 17 (2011) 7777–7780.
[39] H.G. Yua, R. Liu, X.F. Wang, P. Wang, J.G. Yu, Appl. Catal. B Environ. 111-112 (2012) 326–333.